

Equine Hoof Wall Deformation: Novel Aspects Revealed

Benjamin S. Lazarus, Rachel K. Luu, Samuel Ruiz-Pérez, Josiane D. V. Barbosa, Iwona Jasiuk, and Marc A. Meyers*

The equine hoof wall has a unique hierarchical structure that allows it to survive high-impact scenarios. Previous authors have explored the compressive, viscoelastic, and fracture control properties of the hoof wall and suggested that this complex structure plays a vital role in the hoof's behavior. However, the link between the structure and the behavior of the hoof wall has been made primarily with the use of post-fracture analysis. Here, periodic microcomputed tomography scans are used to observe the temporal behavior of the hoof's meso and microstructures during compression, fracture, and relaxation. These results shed light on the structural anisotropy of the hoof wall and how its hollow tubules behave when compressed in different directions, at different hydration levels, and in various locations within the hoof wall. The behavior of tubule bridges during compression is also reported for the first time. This study elucidates several fracture phenomena, including the way cracks are deflected at tubule interfaces and tubule bridging, tubule arresting, and fiber bridging. Finally, relaxation tests are used to show how the tubule cavities can regain their shape after compression.

hoof capsule which provide stiffness,^[3,4] fracture toughness,^[2,5,6] and impact resistance.^[7,8] The role of the tubules in fracture propagation and crack control has been well studied. It was shown that tubules can redirect cracks away from the living tissue at the interior of the hoof and create tortuous fracture paths within the hoof wall.^[2,5,8] Yet, there are still open questions about the configuration of the hoof wall's tubules. For example, the hoof wall contains a well-documented gradient in tubule dimensions with densely packed, smaller, elliptical-shaped tubules near the hoof's exterior and spaced-out, larger, more circular tubules (although all tubules are elliptical) near the interior (depicted in **Figure 1a**). Previous authors have debated whether this is meant to create a barrier for cracks initiating at the hoof's surface,^[2,9] provide a smooth transfer of energy through the hoof wall,^[10] improve the flexural capabilities of the keratinous capsule^[11] (much like the

mechanisms observed in bamboo^[12–16]), or is simply a residue of manufacturing constraints at the proximal generative tissue.^[11] Still, no definitive conclusion has been put forward. Furthermore, while Huang et al.^[4] showed that tubules completely densify by 60% longitudinal strain, correlating to a steep increase in the stress–strain curve of hoof wall material, the highly anisotropic hoof wall experiences multidirectional

1. Introduction

The hoof wall is a highly impact-resistant biological structure with many impact resistant design motifs.^[1] One of the most characteristic features of the hoof wall is the hollow reinforced tubules (approximately 200–250 μm in diameter^[2]) that run from the generative tissue at the top of the hoof wall to the base of the

B. S. Lazarus, M. A. Meyers
Materials Science and Engineering Program
University of California San Diego
9500 Gilman Drive, La Jolla, CA 92093, USA
E-mail: mameyers@ucsd.edu

R. K. Luu, M. A. Meyers
Department of Mechanical and Aerospace Engineering
University of California San Diego
9500 Gilman Drive, La Jolla, CA 92093, USA

R. K. Luu
Department of Materials Science and Engineering
Massachusetts Institute of Technology
77 Massachusetts Avenue, Cambridge, MA 02139, USA

 The ORCID identification number(s) for the author(s) of this article can be found under <https://doi.org/10.1002/ssstr.202200402>.

© 2023 The Authors. Small Structures published by Wiley-VCH GmbH. This is an open access article under the terms of the Creative Commons Attribution License, which permits use, distribution and reproduction in any medium, provided the original work is properly cited.

DOI: 10.1002/ssstr.202200402

S. Ruiz-Pérez
Facultad de Ciencias
Universidad Nacional Autónoma de México
Investigación Científica
Ciudad Universitaria, Coyoacán, Ciudad de México 04510, Mexico

J. D. V. Barbosa
Department of Materials
University Center SENAI CIMATEC
1845 Avenida Orlando Gomes Piatã, Salvador, BA 41650, Brazil

I. Jasiuk
Department of Mechanical Science and Engineering
University of Illinois Urbana-Champaign
1206 West Green Street, Urbana, IL 61801, USA

M. A. Meyers
Department of Nanoengineering
University of California San Diego
9500 Gilman Drive, La Jolla, CA 92093, USA

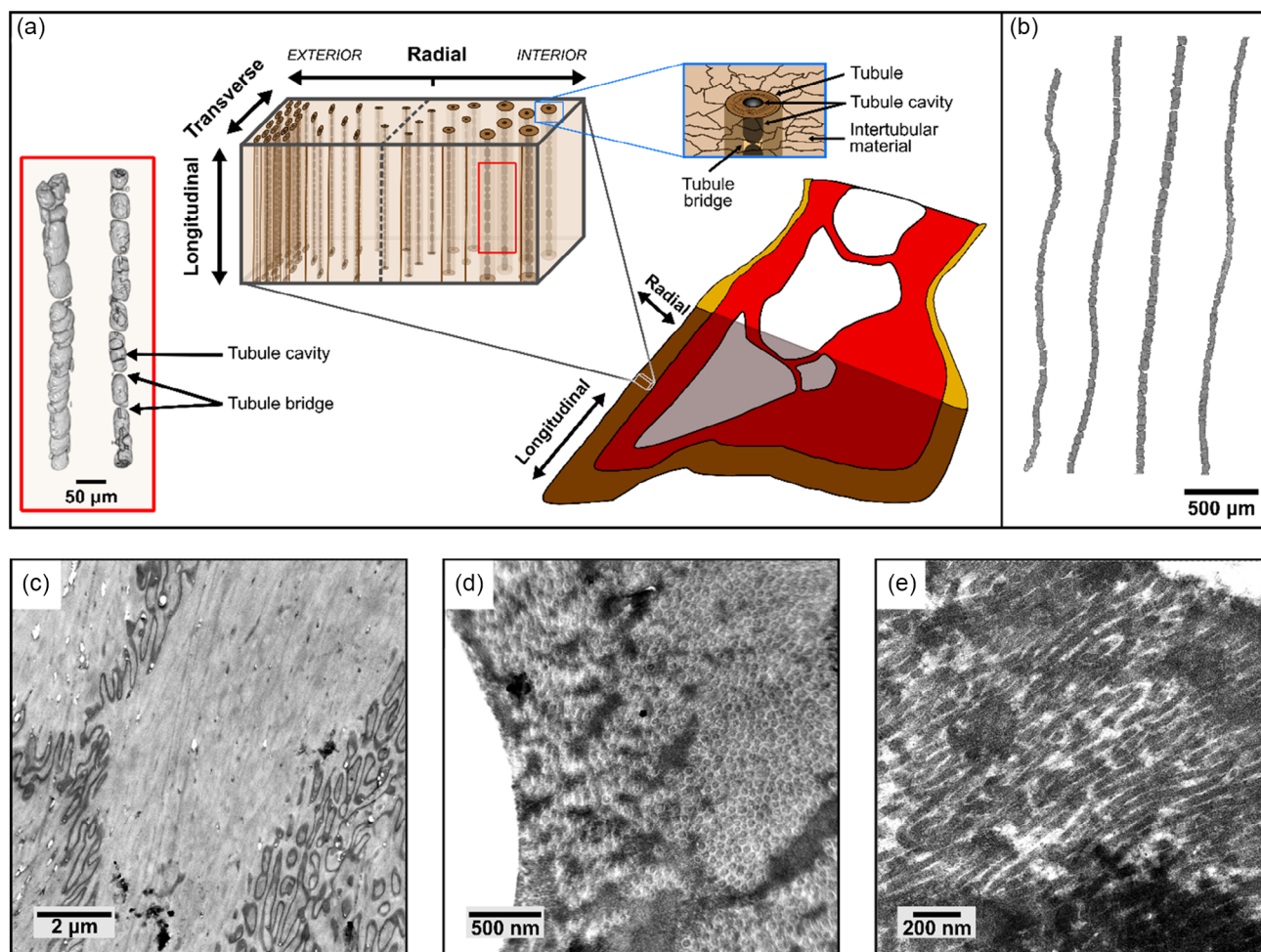


Figure 1. a) Schematic of the hoof showing the orientation of the different axes in the hoof and their nomenclature. Tubule shape, density, and size vary along the radial axis (interior–exterior). The dotted line indicates where interior vs. exterior samples were taken from for compression testing, while the red box shows a 3D rendering of the hollow medullary cavities at the center of the tubules, which are divided into pockets by the tubule bridges; b–e) portray hierarchical features of the hoof wall in decreasing size. b) Individual tubule cavities extracted from microCT scans showing the wavy nature of the tubules. The gaps in the cavities are caused by tubule bridges, material that spans the hollow portion of the tubule. Transmission electron microscopy (TEM) images revealing the submicro and nanoscale structure of the horse hoof wall. On the microscale are cells that form the lamellae and tubular cortical layers of the hoof wall. The sutured interfaces mechanically interlocking these cells can be seen in c), while a d) cross-sectional slice and e) longitudinal view of the nanoscale fibrils that fill the keratinocyte cells are shown as well. For reference, a schematic visualizing the hierarchical structure of the hoof can be seen in the next figure.

loading conditions owing to its complex shape.^[17,18] Also, little is known about the behavior of the tubules when loaded in the transverse and radial directions, which could unlock the mystery of the complex reinforced-composite design of the hoof wall. Previous authors have also debated why the tubules are hollow (isolated 3D renderings of the tubule cavities from microcomputed tomography (microCT) scans are shown in Figure 1b), suggesting that this design would perform better if solid and arguing that its structure is merely a manufacturing constraint.^[2,5]

Bridges traversing the hollow medullary cavity, which is about 40–70 μm in diameter,^[2] at the center of the tubules in the hoof wall were first observed by Kasapi and Gosline^[11] and later by Huang et al.^[4] However, the authors offer no hypothesis regarding the role of these features. Lazarus et al.^[8] identified and quantified tubule bridges, providing a bridge density (with an average

of one bridge every 111 μm along the cavity's longitudinal axis) and an average bridge thickness (10.3 μm). The same study also used post-impact fractography to suggest that these bridges play a role in stabilizing the tubule. The results showed that bridges are one of the first features in the hoof to rupture and that their failure absorbs impact energy, which helps keep the tubular reinforcement intact. However, these experiments provide an incomplete understanding of the mechanical role of bridges in the tubules and their behavior during loading. Furthermore, this failure mechanism was only observed in the dry state, and it has been repeatedly shown that the hoof behaves quite differently when hydrated.

Many other systems in nature, such as bone, tooth, antler, horn, and wood, have evolved tubular structures that play an essential mechanical role in resisting compressive loading. Yet, amongst

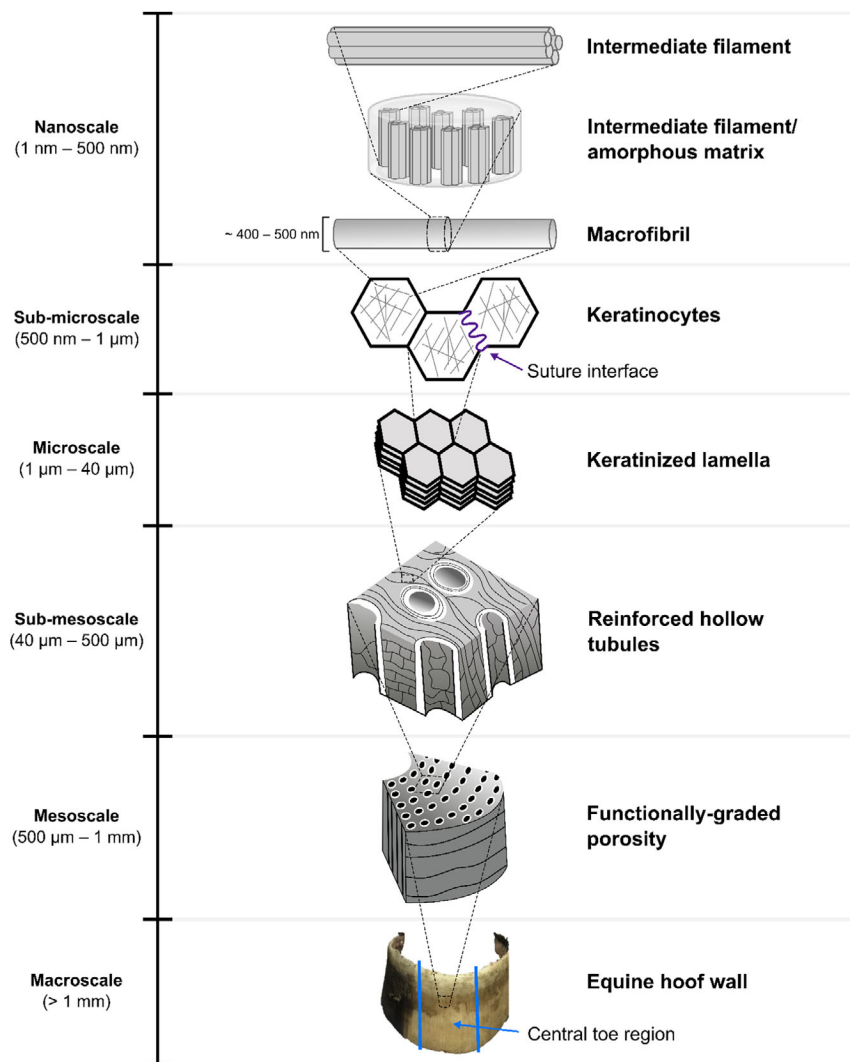


Figure 2. Schematic showing the hierarchical structure of the horse hoof wall including the tubules shown in Figure 1b, the sutured cellular interfaces shown in Figure 1c, and the keratinous fibers that range from hundreds to single nanometers. Figure adapted with permission.^[8]

these, the hoof wall is unique. It is composed of dead cells with sutured interfaces (shown in Figure 1c) that are filled with keratin fibers (shown in Figure 1d,e) and are incapable of repairing and remodeling if the hoof is damaged. The hierarchical structure of the hoof wall is depicted in **Figure 2**. Also, unlike its bony counterparts, the hoof wall is not mineralized and therefore can be much more ductile, particularly when hydrated. As such, the structure of the load-bearing hoof wall has deviated from the architectures of these other materials, incorporating unique design gradients and bridging elements. In this study, 4D microCT is used to provide insight into some of the decades-old questions surrounding the hoof wall's microarchitecture and to provide blueprints for designing engineered composite materials. This technique allows researchers to observe the microstructural deformation behavior of a material as it is occurring, instead of trying to piece together what happens during loading retroactively by observing the surfaces of failed samples. As a result, time-dependent phenomena such as buckling and bending, which may relax after

testing or be interrupted by rupture and critical failure, can be observed.

Furthermore, periodic microCT testing can be used to capture time-dependent relaxation behavior to understand the structure-induced viscoelasticity of a material. Lazarus et al.^[8] modeled the viscoelastic nature of hooves under compression and found that meso and microscale features of hoof keratin allow it to relax faster than other keratinous materials like hair. Using periodic microCT, we can directly observe the relaxation behavior of hoof wall features and attach the microstructural deformation events to the macroscale behavior. A similar approach can be used to visualize how cracks propagate through the hoof wall and how this plays into the results of previous authors.^[2,5,7,8]

This study is divided into three parts. The first (Section 3.1) part uses coupling of microCT with compression tests to study the effect of hydration, loading orientation, and location (interior vs. exterior) on the deformation behavior of the hoof wall's internal architecture. The second (Section 3.2) portion focuses on the

relaxation behavior of the hoof wall and how its microstructure responds after a loading event. The final section (Section 3.3) utilizes periodic microCT with fracture toughness tests (using a compact tension configuration) to analyze the interplay between the structural features in the keratinous wall and its fracture behavior.

Earlier studies have noted variations in the hoof wall's macroscale compressive properties with hydration (keratin becomes significantly more ductile when hydrated^[4,18,19]), loading orientation (compression tests have shown that hoof wall is quite anisotropic^[4,19]), and location (the inner portion of the hoof wall tends to be more compliant^[19]). Numerical studies of the hoof wall have built on some of these experimental results, focusing primarily on hydration and how it can increase the macroscale principal strain of the hoof during loading^[20] and reduce its elastic modulus.^[20,21] Ram horns have a similar structure to the horse hoof wall and are also composed of keratin. However, they bear tubules that lack a reinforced region and bridges and are oriented perpendicular to the loading direction. When compressed, the horns absorbed the most energy when loaded radially, and the authors contributed this to the lengthwise collapse of the hollow tubules. Finally, the hoof's microstructure varies by location, with tubules changing in shape, density, and size along the radial axis. Ultimately, this means there is more reinforcement near the edge of the hoof wall than the interior.^[2] Several hypotheses based on these previous studies will be explored in Section one: 1) higher moisture content in the hoof wall will lead to ductile failure of the microstructure including tubule collapse and buckling of the tubule bridges, while lower hydration states will lead to catastrophic plastic failure, such as cracking and bridge rupturing; 2) tubules compressed along the radial and transverse directions will collapse at lower strains and more readily than tubules compressed in the longitudinal direction; 3) the microstructure of the hoof wall, including tubule bridges and shape, will exhibit anisotropic behavior and bridges may play a role in reinforcing the tubules against loading perpendicular to their axis; and 4) the microstructure of interior and exterior samples will behave differently during compression.

Keratinous materials are highly susceptible to hydration, and many biological systems take advantage of this. For example, the feather rachis's foam core swells when exposed to water after bending deformation, helping induce shape recovery of its entire cross-section,^[22] while tubules in ram horns reduce the formation of shear bands and reform after collapsing.^[23] Section two will use stress relaxation tests to examine the following: 1) higher initial moisture content and wet environments will increase the rate of volume recovery after the hoof wall undergoes compression; 2) repeated loading with recovery periods in between on the hoof wall helps to dissipate energy and maintain tubule structural integrity overall; this is also strongly influenced by moisture content; and 3) the tubular structure and bridges will recover their shape after deformation, especially under hydrated conditions.

The fracture resistance of the horse hoof wall has been well documented^[2,4,5,7,8], however, the cracking behavior of the hoof wall has always been determined retrospectively using post-test fractography. In this study, the progression of a crack will be observed as it propagates through the hoof wall. These tests will be used to evaluate these hypotheses: 1) the tubule reinforcement

redirects incoming cracks, increasing the tortuosity and overall length of the fracture; 2) cracks get trapped by the microfeatures of the hoof wall, such as the lamellae and cortical layers, which can lead to fiber bridging, crack splitting, and crack arrest; 3) hydration will increase crack blunting in the hoof wall and change its fracture behavior; and 4) the fracture behavior of the hoof wall will resemble that of the compact tension tests performed by Lazarus et al.^[8] on hoof-inspired 3D-printed materials.

2. Experimental Section

2.1. Sample Preparation

Hoof samples were obtained from the University of California, Davis, Veterinary Department. They were taken from the rear hooves of a three-year-old female racehorse weighing 461 kg that died from musculoskeletal injuries. The hooves were removed from the corpse within 4–24 h and were then refrigerated for 24–48 h before being frozen at -20°C . The keratinous hoof capsule was removed from the hooves before being roughly cut into strips with a rotary saw. Compression and relaxation samples were machined into cubes using a tabletop saw, while compact tension coupons were processed at the UCSD Campus Research Machine Shop. Samples were tested at three different hydration levels: hydrated, ambient conditions, and dry. All samples were oven dried at 100°C for 72 h. Immediately after being removed from the oven, dry samples were sealed in two plastic bags with desiccant for transportation. Hydrated samples were soaked in water for 24 h before testing, while ambient condition samples were subject to about 75% relative humidity prior to testing. This corresponds to a moisture content of about 18.2%.^[24]

2.2. Transmission Electron Microscopy

Transmission electron microscopy (TEM) samples were prepared from slices of hoof wall taken from the central toe region (highlighted in Figure 2). Samples were fixed in a 2% glutaraldehyde solution in sodium cacodylate (CaCO) buffer for 2 h at room temperature and then washed in a CaCO buffer three times for ten minutes each. They were post-fixed in a 1% osmium tetroxide solution, with 0.8% potassium ferricyanide and 5 mM calcium chloride in CaCO buffer, for an hour, protected from light. They were then washed again in the CaCO buffer three times for ten minutes each. Following the wash, samples were dehydrated in a series of increasingly concentrated (30%, 50%, 70%, 90%, and 100%) acetone solutions at room temperature for 10 min in each step. The final step was performed twice before the sample was submerged in super-dry acetone. Samples were then infiltrated with PolyBed 812 resin at room temperature and constant slow agitation, for at least 6 h each, in the following proportions: 1) resin/super dry acetone molar ratio 1:2; 2) resin/super dry acetone molar ratio 1:1; 3) resin/super dry acetone molar ratio 2:1; 4) resin/super dry acetone molar ratio 3:1; and 5) pure resin.

Each sample was assembled in a Beem capsule and polymerized for 60 h in an oven at 60°C . Samples were scanned using a JEOL (Tokyo, Japan) TEM-1230 transmission electron microscope.

2.3. Periodic Microcomputed Tomography

Mechanical testing with periodic microcomputed tomography experiments was performed at the Lawrence Berkeley National Laboratory Advanced Light Source on beamline 8.3.2. Three different tests were performed on hoof samples: compression tests, relaxation tests, and compact tension tests. These tests are performed using custom-made testing apparatuses designed by beamline scientists. A 1000 N load cell testing machine is housed in a stainless-steel chamber (Figure 3a,b) with three windows for accessing the sample and for the X-rays to pass through. This apparatus is placed inside the beamline hutch, which uses X-rays siphoned from the synchrotron to perform microcomputed tomography scans of mechanically loaded samples. Since movement during imaging introduces noise and error, mechanical tests are paused periodically for scans to be taken. Owing to the length of time required for each test and high demand for beamline access, only one or two samples could be tested for each condition. However, within a single scan, the behavior of dozens of tubules could be observed. The goal of these tests was not to evaluate the mechanical properties of the hoof wall, which have been determined elsewhere (i.e., fracture toughness,^[2,5–7,24] strength,^[4] elastic modulus,^[4,8,18,19] or relaxation behavior^[8]) but rather to understand the behavior and failure mechanisms of the features in the hoof wall, which are discussed in these studies but never visualized.

Scans were taken at 22 keV using a camera exposure of 225 ms, an Optique 10× lens, a 20 μm LuAGb scintillator at 130°, a focus of 17.345 mm, and a tilt of 0.579 μm. Scans took around 7 min to run. The projections were reconstructed with custom software (<https://microct.lbl.gov/software>) produced by ALS beamline scientists. The reconstructed images (slices) had a voxel size of 0.639 μm³ and were processed and analyzed with Fiji.^[25] First, the individual slices were imported as image sequences and integrated into three-dimensional (3D) stacks. Then, stacks were resliced according to the desired view of the hoof wall tubules (transverse, radial, or longitudinal), avoiding interpolation. To compare the behavior of a sample as it was compressed, features were tracked across equivalent (corresponding) microCT slices. For example, this was used to assess tubule bridge morphology changes between different strain intervals on the same sample. To that end, sample features that were in roughly the same horizontal, vertical, and stacked (depth) locations and had similar surrounding characteristics between testing conditions were regarded and measured as four-dimensional (4D) corresponding features. Finally, to improve visualization and for figure generation, the microCT stacks were subjected to further processing with Fiji. In the case of the two-dimensional (2D) figures, this processing consisted of background subtraction (30–90 px rolling ball radius), 0.1% contrast enhancing, and, specifically for compact tension scans, an additional

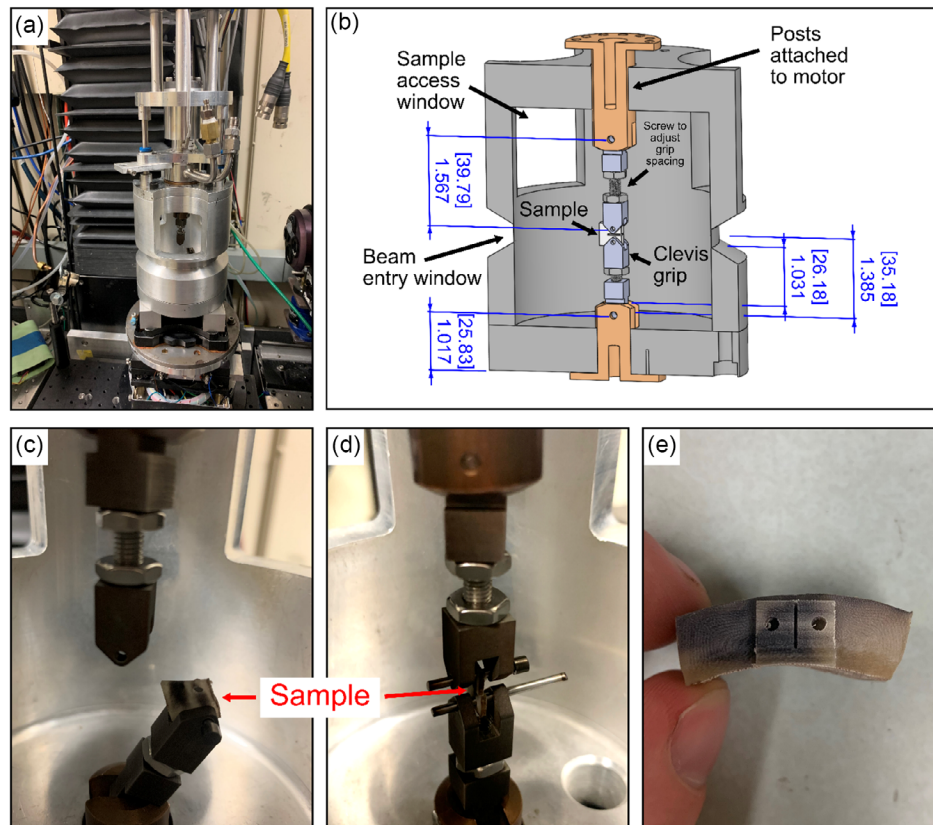


Figure 3. a) Image of the compact tension rig inside the hutch at beamline 8.3.2 at Lawrence Berkeley National Laboratory's Advanced Light Source (synchrotron); b) schematic showing the design for the clevis grips and compact tension samples with measurements listed in [mm] and inches; c) closeup shots of a partially loaded; d) fully loaded sample in the clevis grips; and e) image of a nearly complete compact tension sample showing its location and orientation in the hoof wall.

manual segmentation step to highlight fractures (shown in white) from the rest of the sample (shown in gray). Conversely, in the case of the 3D renderings of tubules, the processing was customized based on the properties of the stacks and consisted of 0.1% contrast enhancing, noise reduction 3D filtering, default black and white pixel thresholding, morphological 3D eroding and dilating, 3D hole filling, and size-based object filtering. These 3D operations were performed using the 3D ImageJ Suite.^[26] Global 3D visualization and snapshot generation of tubule morphology was performed using Fiji's Volume Viewer plugin. The 3D renderings in this manuscript visualize the hollow portions (air) within the sample such a tubule cavities and cracks. In the 2D slices, the hollow regions are shown in dark gray, while the hoof material is shown in light gray.

2.4. Compact Tension Tests

Custom-made clevis grips were prepared to attach the sample to the tensile rig in the microCT beamline (Figure 3). A screw was used to attach the clevis grips to the testing machine posts so that the grip clearance could be adjusted for future beamline users. Samples were extended at a crosshead speed of $25 \mu\text{m s}^{-1}$, and scans were performed at intervals of $100 \mu\text{m}$ until the crack propagated entirely through the sample. Compact tension samples were machined out of strips of hoof wall from the central toe region (Figure 3e) following ASTM D5045 with the crack oriented along the radial axis using a Haas TM1 (Haas, Oxnard, CA, USA). Aluminum jaws were used to cut a pocket in the shape of the sample and then an endmill to cut the pieces. Care was taken to ensure that small cuts were made, and samples were cooled with water during cutting. Owing to the narrow thickness of the hoof wall, samples could only consistently be cut to $10 \times 10 \text{ mm}^2$. To facilitate tomography scans, 1 mm thick samples were used, allowing a good signal to be transmitted to the detector. A precrack was introduced at the end of the slit using a razor blade.

2.5. Compression Tests

Samples $5 \times 5 \times 5 \text{ mm}^3$ in dimensions were taken from the central toe region (highlighted in Figure 2) of the hoof wall (as shown in the callout in Figure 1a) in the same region as the compact tension sample shown in Figure 3e. Samples were scanned prior to testing and then compressed at a strain rate of 0.005 s^{-1} to intervals of 10% or 20% and then held at that strain while they were scanned. Samples were allowed to relax for one minute prior to scanning to minimize movement during imaging. Such imaging was performed either until 80% strain or until the sample failed. The setup for this test was the same as that of the compact tension test shown in Figure 3; however, the adjustable clevis grips (depicted in light grey in Figure 3b) were replaced with flat, stainless steel compression platens. Samples were tested in hydrated, dry, and ambient conditions.

Ambient samples were prepared to be tested in each of the three axial directions: longitudinally (along the tubule axis), radially (along the exterior-interior axis of the hoof), and transversely (sometimes referred to as circumferentially, this is along the hoof wall's thickness). To understand how the different tubule

geometries and configurations that exist through the hoof wall's thickness behave during loading, ambient condition samples were taken from the interior and exterior of the hoof wall (as indicated by the dotted line in the callout of Figure 1a) and compressed along the longitudinal axis for comparison. Load–displacement data gathered from the compression tests were used to construct stress–strain curves. The elastic modulus was calculated from a tangent line along the linear regime of the first compression interval of each sample.

2.6. Relaxation Tests

Relaxation samples were prepared in the same manner as those for compression tests. Samples were scanned prior to testing (the initial samples), then loaded monotonically at a strain rate of 0.005 s^{-1} to set strains (20%, 40%, 60%, and 80%) and scanned immediately. Then, the load was released, and another scan was initiated after 5 min. One sample was compressed sequentially, reaching 80% strain in 20% strain increments with relaxation periods between loadings. Samples were also tested at two different initial hydration conditions (dry and hydrated) and two different relaxation conditions (ambient or water immersed). All samples were initially oven dried at $100 \text{ }^\circ\text{C}$ for 72 h and then sealed similarly to compression test samples. Hydrated samples were soaked in water prior to experiments until the samples reached a water content of $17.5\% \pm 1.26\%$, calculated by comparing the weight of the dry sample versus after soaking. In ambient relaxation conditions after loading, the samples were left in an open container exposed to ambient conditions. In water-immersed relaxation condition during loading, moisture was consistently applied to the sample during the beamline experiment by covering the wet, hydrated sample with plastic wrap. After loading, the sample was then submerged in water. Sample dimensions were tracked during recovery using digital calipers routinely for the next 12 h.

2.7. Statistical Analysis

When more than one sample is presented, errors bars indicate the standard deviation of the sample set. Plots are generated with OriginPro, 2019 (Northampton, Massachusetts, USA) and ggplot2^[27] in R.^[28]

3. Results and Discussion

3.1. Compressive Behavior

When compressed, tubules tend to behave as a cohesive unit, likely due to the reinforcement that surrounds the medullary cavity, buckling into an “S” shape. In untested hooves, tubules often exhibit some waviness along their longitudinal axis, undulating back and forth in both the radial and transverse directions (a schematic of the hoof wall's axes nomenclature is shown in Figure 1a). This initial waviness (Figure 1b) provides a template for the tubules' motion during compression. The bowed portions of the tubules become exaggerated, and the amplitude of the waves increases as the hoof is compressed longitudinally. Buckling is the most common failure mode of engineered

composite materials in compression, and it generally is accompanied by shear band kinking (microplastic buckling), where lateral cracks develop in the reinforcing elements.^[29–31] Such failure leads to a precipitous drop in stress and the overall toughness of the composite. However, in hydrated and ambient hoof samples, the tubules buckled significantly without exhibiting kinking. This behavior has been reflected in the measured stress–strain curves (Figure 4) as well as those of previous studies, where the stress level continues to rise throughout compression. Such a constitutive response is likely because the reinforcement is composed of a relatively soft and ductile polymeric material.

The mechanical results of this study (shown in Figure 4) align well with those of other studies.^[4,18,19] For example, samples from the hoof’s exterior were stiffer and generally reached higher stress values than interior samples under the same conditions. Also, samples compressed in the radial direction were initially more compliant than those compressed in the other two directions. However, after ≈ 0.2 strain, the stress values for radially compressed samples rise above those of both longitudinally and transversely compressed specimens, suggesting earlier densification of the tubule cavities. The elastic moduli for each sample fall comfortably in the range determined by Lazarus et al.^[8] which uses more robust sample sizes.

The cavity bridges provide a degree of resistance to tubule collapse during compression. Figure 5a shows a longitudinal cross-section of the same interior tubule being compressed radially at different strains. After 10% strain, small amounts of bridge and tubule wall deformation can be seen throughout the tubule, with slightly more seen in the top portion of the tubule where the bridge density is lower. At 20% strain, nearly the entire tubule has collapsed in the region with fewer bridges, while small pockets survive between the compacted bridge material in the lower portion of the tubule. Figure 5b shows a perpendicular cross-section of several exterior tubules compressed in the transverse direction. Much like the radially compressed tubules shown in Figure 5a, these tubules collapsed more in areas with less bridging and experienced buckling of the tubule wall in the unsupported pockets. Meanwhile, in regions with more bridge support, bridges were observed buckling and deforming into characteristic “S” shapes, while the tubule walls maintained their geometry.

3.1.1. Variations by Water Content

The water content of the hoof significantly affects the hoof’s mode of failure. In agreement with,^[4,8] it is found that hydrated hoof tubules buckle under compression, whereas a dried hoof

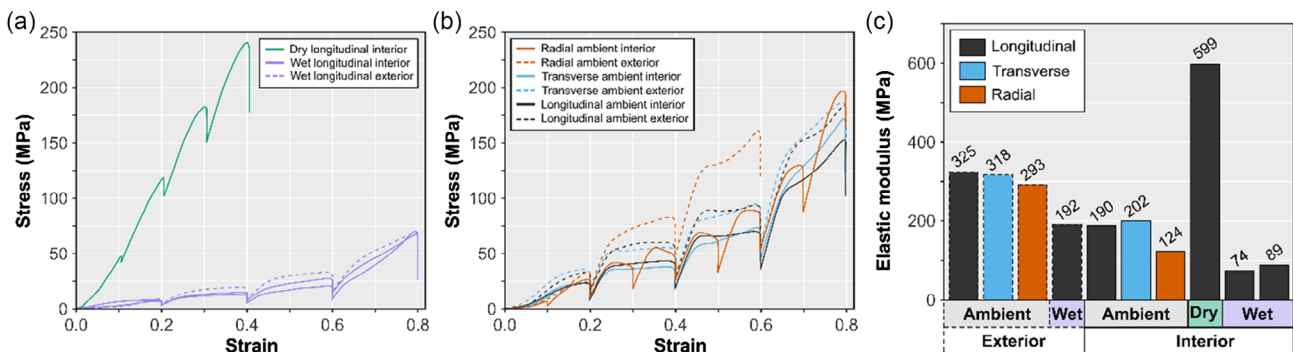


Figure 4. Mechanical data from each compression test. a) Stress–strain curves of wet and dry samples compressed longitudinally. The periodic drops in stress arise from relaxation that occurs while the sample is being scanned; b) samples in ambient conditions compressed along each axis from both the interior and exterior portions of the hoof wall; and c) elastic moduli of the sample from each compression condition.

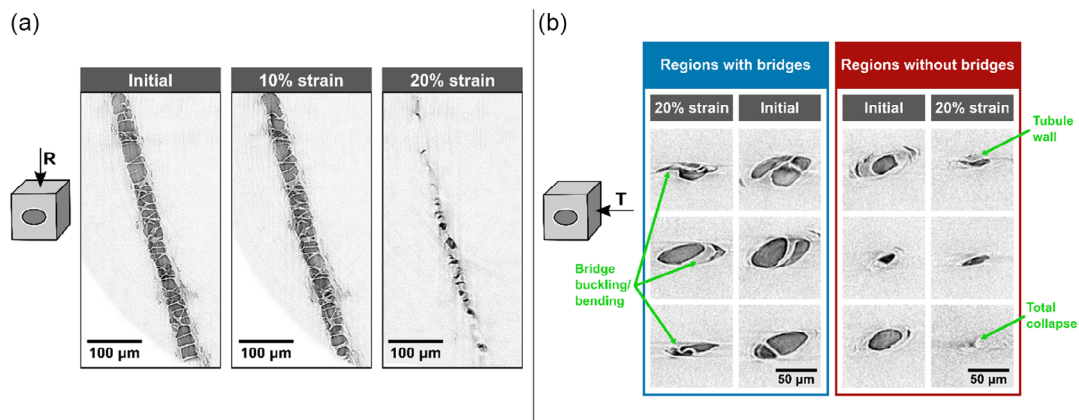


Figure 5. a) Microcomputed tomography (microCT) scans of tubules hydrated at ambient conditions compressed radially, showing how the tubules collapse first in regions with less dense bridging and b) MicroCT scans of tubules compressed in the transverse direction, highlighting how bridges can help prevent collapse, relative to regions without bridges (scale: each of the microCT images shown in this panel is a square of $100 \times 100 \mu\text{m}$). In both (a, b), the load is being applied to the tubules in the images from the left and right of the page.

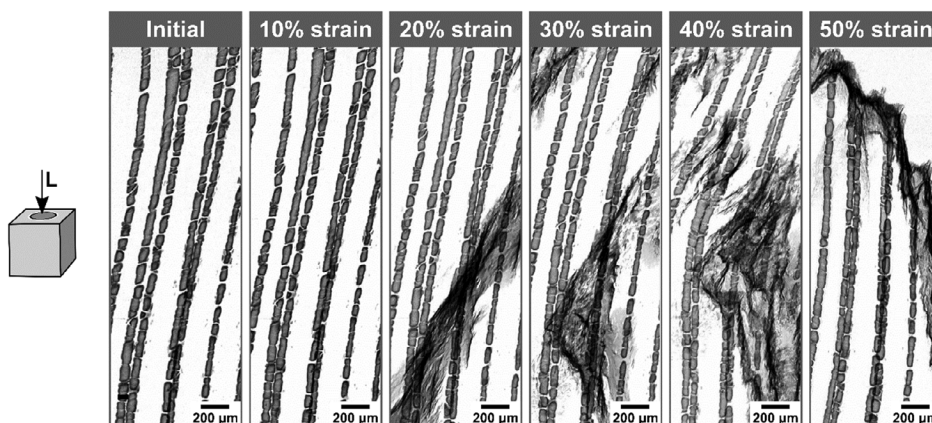


Figure 6. Three-dimensional renderings of microcomputed tomography (microCT) scans taken of dried hoof wall samples compressed in the longitudinal direction at intervals of 10% strain. Dark jagged features beginning at 20% strain are cracks propagating within the sample.

cracks before the microfeatures experience much deformation. **Figure 6** shows the progression in increments of 10% strain of a dry hoof sample cracking under compressive load. Formation of large black splotching corresponds to cracks weaving between the tubules and tubule bridges, initiating between 10% and 20% strain. Tubules begin to bend toward the top of the field of view at around 30% strain until a clean fracture occurs at 50% strain, shearing off the tops of the tubular cavities.

A direct comparison of a wet and dry hoof is demonstrated in **Figure 7**, showing the initial tubular cavities and their configuration at 30% strain. At 30% compressive strain, the dry hoof cavities show minimal deformation, but cracks form around the cavities. As for the wet hoof sample, no cracks are observed. Instead, parts of the cavities begin to densify as the tubules deform into an “S” shape. Very little deformation was observed in the bridges of dry samples, even just before the onset of fracture, as shown in **Figure 8**.

3.1.2. Variations by Location

In agreement with the mechanical results shown in **Figure 4**, Leach^[19] found that the inner wall had a much lower modulus of elasticity than the outer wall, reaching values of 62.5% when compressed along the tubules and just 51% when tested in the other two directions. Leach also suggested that the outer wall has a resilience that is 1.5–2 times greater than that of the inner wall.

The microCT results showed that tubules in interior samples compressed longitudinally collapsed at lower strains, being nearly completely densified by 40% strain. Meanwhile, exterior samples were often able to maintain their internal features until 60% strain. Interestingly, tubule features in the exterior of the hoof wall show noticeable, progressive damage during compression, including cavity collapse and bridge buckling. Interior samples, conversely, exhibited minimal deformation before collapse.

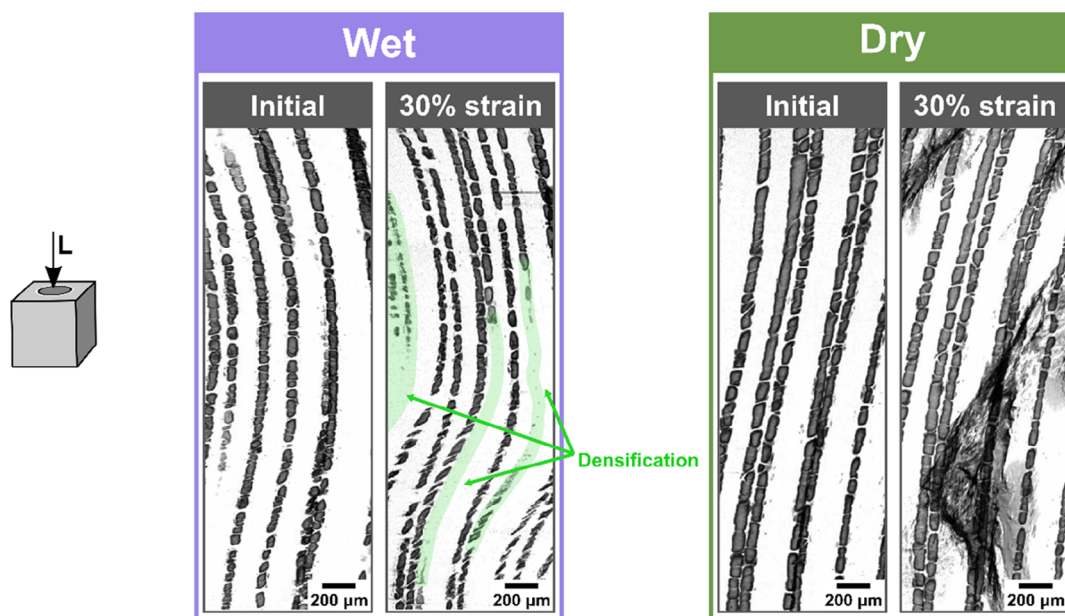


Figure 7. A side-by-side comparison of microcomputed tomography (microCT) scans of wet and dry samples compressed to 30% in the longitudinal direction. Wet samples exhibit much more tubule buckling and cavity collapse, while dry samples form diagonal cracks.

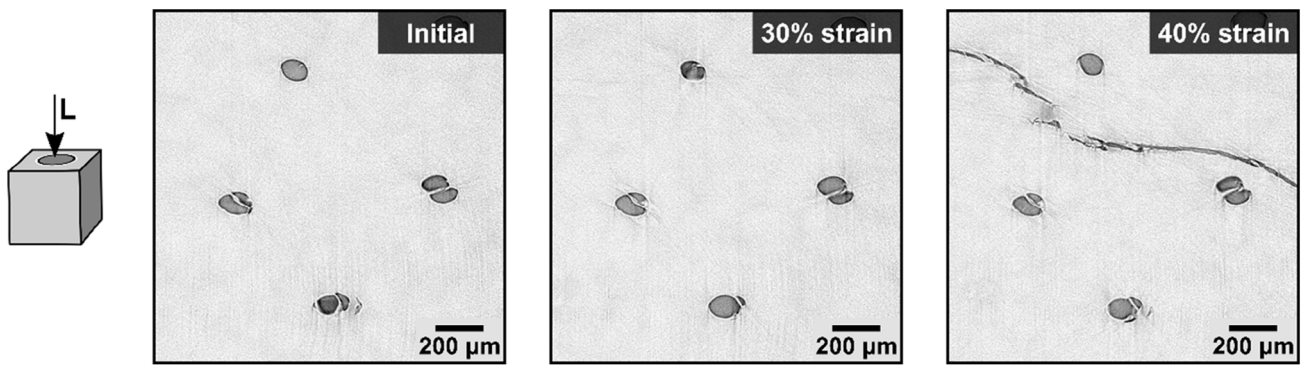


Figure 8. Microcomputed tomography (microCT) scans of a dry sample compressed in the longitudinal direction showing cracking but minimal deformation of the tubule bridges.

These phenomena can be seen in **Figure 9**, which shows tubules compressed in the longitudinal direction. However, this trend is consistent among tubules compressed in all directions. This observation supports the mechanical findings of Leach.^[19] One possible explanation for this behavior could be the effect the difference in tubule size and shape has on the bridge behavior. In the larger interior tubules, the bridge span is longer, particularly in the radial direction (along the minor axis of the more elliptical tubules), which could reduce the resistance provided by the tubule bridges relative to the smaller, elliptical tubules at the exterior.

3.1.3. Variations with Loading Direction

Thomason et al.^[17] used strain gauges mounted on living horses' hooves to determine that the hoof wall experiences significant lateral biaxial deformation during locomotion. Biaxial strains primarily arise due to heel spreading and load transfer between the exterior and interior portions of the hoof. The authors regard the

hoof wall as a multidirectional composite that can withstand strains in every loading orientation. Leach^[19] and Huang et al.^[4] found that the hoof's properties vary by loading orientation and that, surprisingly, the hoof can be stiffer perpendicular to the hollow, reinforcing tubules. Thomason et al.^[17] suggest that this behavior is meant to resist these biaxial loads. Further, Huang et al.^[4] found that the hoof wall absorbs more energy when compressed in the radial direction relative to the other two orientations. However, beyond these macroscale mechanical observations, there is little understanding of why this behavior arises from the hoof wall's microstructure.

Tubules compressed in the radial direction collapsed at a lower imposed deformation than the others. Figure 5a shows how tubules compressed in the radial direction are nearly entirely densified by 20% compression, while Figure 5b (transverse) and 9 (longitudinal) show tubules compressed in different directions retaining most of their structural integrity at 20% strain. A cross-section of this phenomenon can also be seen in **Figure 10a**.

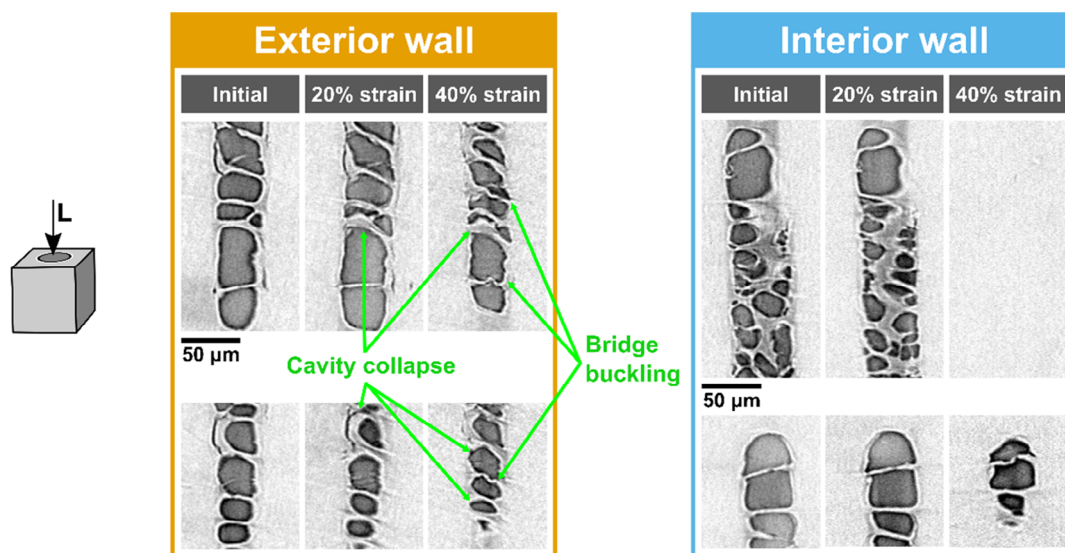


Figure 9. Images extracted from in situ microcomputed tomography (microCT) scans showing longitudinal cross-sections of samples compressed along the tubule axis. Images on the left show individual tubules from exterior samples, while those on the right show those of interior samples (scale: each of the microCT images shown in this panel is a rectangle of 100 μm width).

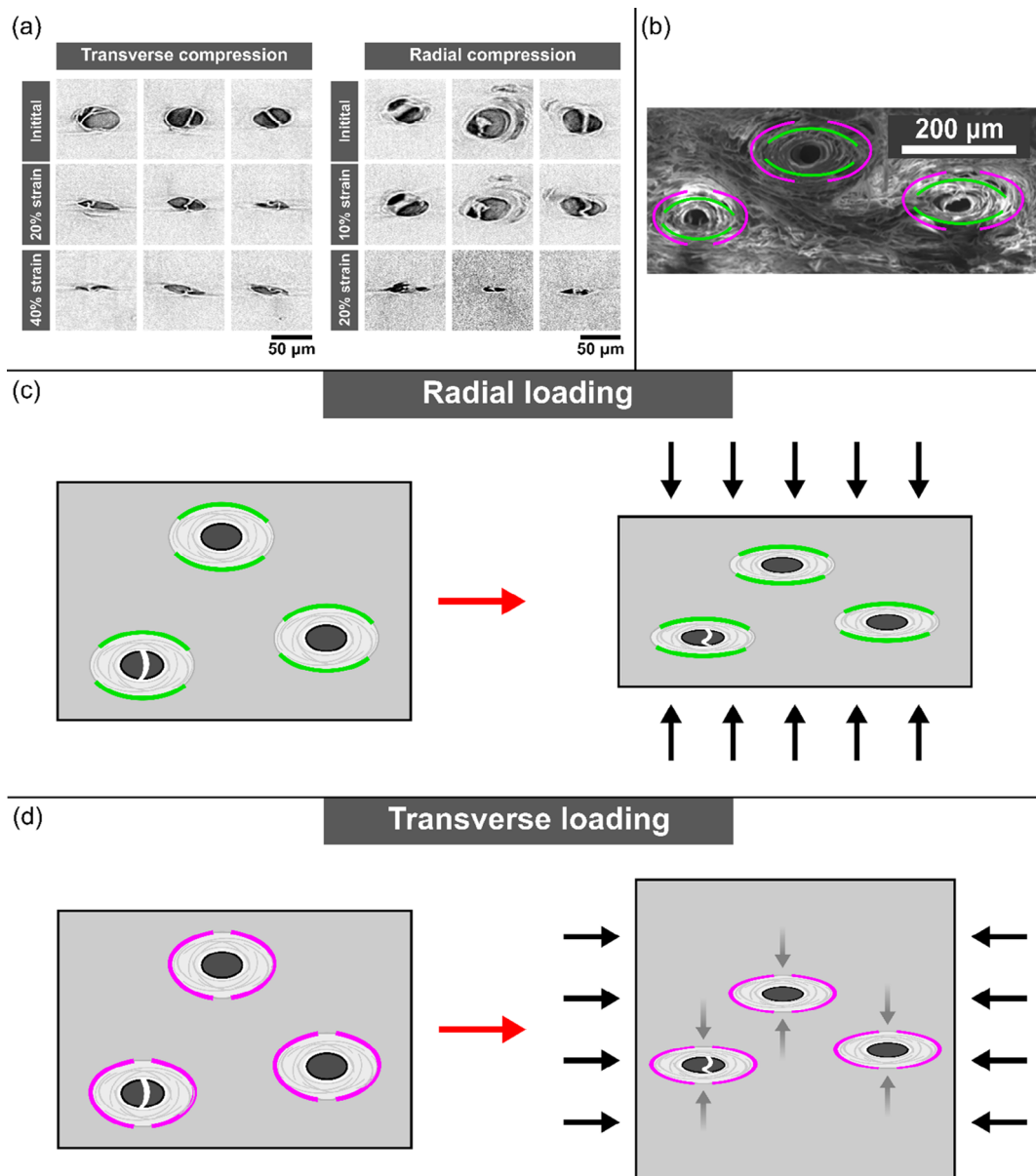


Figure 10. a) Extracted images from microcomputed tomography (microCT) scans of individual tubule cavities being compressed in the transverse direction to 20% and 40% strain (scale: each of the microCT images shown in this panel is a square of $100 \times 100 \mu\text{m}$); b) scanning electron microscope image showing the fibers composing the tubule walls with fiber orientation perpendicular to radial loading emphasized in green and fiber orientation perpendicular to transverse loading emphasized with pink; c) samples compressed in the radial direction collapse easily along the minor axis of the tubules partially due to the weakness of the tubule wall's fiber orientation; and d) the arched fibers perpendicular to the tubules major axis resist transverse loading and instead tubules are compressed by the expansion of the matrix.

The scans revealed that regardless of the compression direction, tubules almost always prefer to collapse along the radial axis (which corresponds to the minor axis of the elliptical tubules). This behavior is particularly surprising in samples that are compressed in the transverse direction (Figure 10a). Much like samples compressed in the radial direction, bridge buckling was observed, while regions without tubules collapsed at lower strain values. This finding suggests that the tubules are more resistant to loads in the transverse direction. There are several possible factors that could lead to this modality. One reason is that the

elliptical tubules have more reinforcement along the transverse axis than in the radial direction, increasing the transverse stiffness of the tubules in that direction. Beyond the sheer quantity of reinforcement, the configuration of the reinforcement might also play a key role. Kasapi and Gosline^[2] observed variations in the intertubular intermediate filament (IF) orientation through the hoof wall's thickness. However, regardless of location, tubular fibers tend to “flow” around the hollow medullary cavity. The result of this arrangement is that more fibers that compose the tubule walls are oriented in the transverse direction and form

a reinforced arch along the major axis of the tubule, further stiffening the tubules against transverse loading (Figure 10b). During radial compression, the tubules collapse easily along the flattened curves (emphasized in green) formed by fibers along the tubule's long side (Figure 10c). This behavior likely occurs during transverse compression as well because the softer inter-tubular matrix material is more easily compressed than the fibrous arches along the major axis (emphasized in pink). As the matrix compresses, it expands laterally, pushing on the walls of the tubule in its weakest orientation, the radial direction (Figure 10d). These results align with the findings of Huang et al.^[4] and Leach,^[19] who found that macroscale hoof samples are stiffer in the transverse direction than in the radial direction. Furthermore, their results show that during compression in the longitudinal and transverse directions, samples plateau at around 50 MPa between $\approx 2.5\%$ and 40%. Radially compressed samples, on the other hand, experience a linear increase in stress over this interval before experiencing a steeper stress–strain relation, which aligns well with the assertion that tubules densify more easily in this orientation. The tubule bridges are likely meant to compensate for this radial weakness. Most bridges are oriented along the radial axis, providing resistance to collapse and absorbing energy by buckling when tubule densification occurs.

The role of the hoof tubules and their hollow medullary cavities have long been debated. It had been suggested that the hollow cavities are meant to transport moisture through the hoof or provide resistance to bending while reducing the overall weight of the hoof, only to be disproven.^[11] Huang et al.,^[4] Lazarus et al.,^[8] and Kasapi and Gosline^[2,5,7,11] showed that the tubule walls act as reinforcement, control crack propagation, and absorb energy via debonding from the matrix. Yet, the role of the hollow center, and its recently described bridges, remained a mystery. Here, we propose the following explanation regarding the function of these features and their behavior. The cavities are meant to act as collapsible elements that can absorb strain energy during compression and, when the hoof is sufficiently hydrated, sustain plastic damage before the rest of the hoof wall. Due to the elliptical shape and fiber alignment of the reinforcement around the cavities, the tubules are weaker in the radial direction and prefer to collapse along this axis regardless of the compression direction. To improve the energy absorption of this failure mechanism, bridges span the tubule cavity, generally oriented along the radial axis, and buckle as the tubule collapses. These contorted bridges may also have the added benefit of helping the tubules recover their shape after collapsing. Predictably, the larger tubules at the interior of the hoof collapse at lower strains than the smaller ones near the exterior.

This failure mode may be preferable because the more hydrated tubules near the interior are more capable of recovering and, thus, it is ideal for them to collapse first. Since the hoof wall cannot remodel and repair itself, it would be detrimental to have all the cavities collapse at the same stress level, effectively making the fail-safe cavities a one-time use feature. To ensure that this does not happen, the thickness, orientation, and dimensions of the tubule bridges vary throughout the medullary cavity. The result is that different tubules and even different regions within a tubule collapse at different strains, beginning with the most recoverable, hydrated tubules at the interior. On the macroscale, the result is a smooth stress plateau until 40% strain, during

which only a few regions of the tubule cavities collapse at a time. Thomason et al.^[17] found that the principal strains experienced within the hoof change during a horse's gait are often oriented at an angle to both the tubules and intertubular material and can vary between horses owing to differences in hoof geometry, stance, and size. As a result, complex loads can be experienced within the hoof. The distribution of bridge angles, thicknesses, and spacing has the added benefit of being well adapted to handling loads from any direction.

3.2. Relaxation Behavior

The hoof wall displays significant viscoelastic behavior.^[1] Tomographic imaging provides a glimpse into the behavior of tubule cavities as they relax and recover from loading. **Figure 11** shows two hydrated hoof samples, one sample compressed monotonically to 60% and released and another sample that experienced incremental compression and relaxation cycles up to 80% strain. Figure 11 displays a section of select tubules from each sample at each step. In the sequentially loaded sample, there appears to be little to no deformation change during 20% strain, 40% strain, and their respective relaxation periods. By 60%, the sample begins to bend, behaving similarly to the hydrated compression tomography experiments. The relaxation period that follows the compression step to 60% shows the cavities bending back to their original shape, even within a few minutes. At 80% strain, the bending pattern seen at 60% strain is accentuated. Likewise, the relaxation period allows the cavities to recover and bend back. However, for the monotonically compressed sample, cavities collapse and no longer appear once compressed to 60%. This behavior is dissimilar to the sequentially loaded sample, where it seems that the sample's cavities did not collapse as easily. However, upon relaxation, a few of the cavity sections begin to reappear, implying that the tubules are stretching back out after being compressed rapidly. Not only does the sequentially loaded sample visually show an impressive recovery behavior, but it also shows a stark decrease in maximum stresses experienced. At 60% strain, the sequentially loaded sample experiences a maximum stress of 43 MPa, which is significantly less than the monotonically compressed sample, 81 MPa, which is even greater than the maximum load achieved at 80% strain with the sequentially loaded sample. Additionally, during 60% compression, the monotonically compressed sample stress relaxes by 44.4% within 593 s, whereas the sequentially loaded and relaxed sample relaxes by 53.5% within 500 s. These findings correlate strongly with the results reported by Lazarus et al.^[1] and provide supporting evidence that the hoof wall does have the ability to quickly dissipate compressive stresses through viscoelastic relaxation at the mesoscale. As previously suggested, such dissipation is particularly advantageous for the repeated loadings a galloping horse would experience, where preventing a build-up of strain could contribute to the hoof wall's durability.

3.2.1. Hydration Specific Behavior

Water content plays a significant role in the relaxation properties of the hoof wall.^[8] The relaxation of the hoof wall was studied in the longitudinal direction, the predominant loading direction in

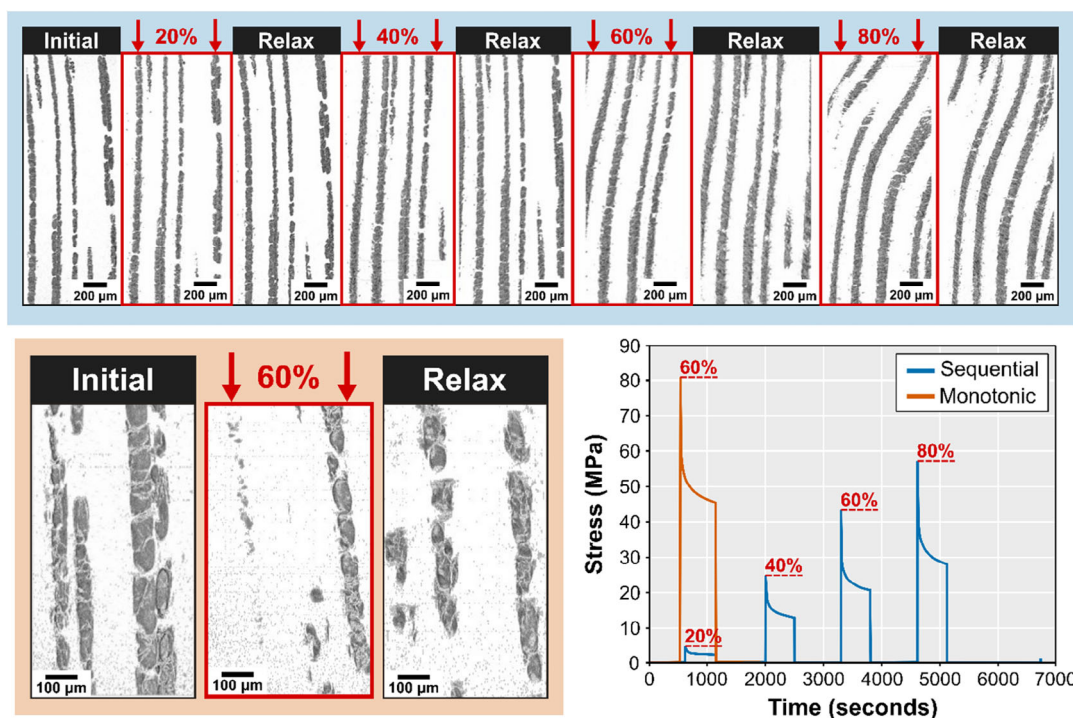


Figure 11. Comparison between the sequentially and monotonically loaded relaxation samples showing the progression from initial states through compression and relaxation periods. Plots of compressive stress (MPa) over time (s) for the two samples are depicted alongside. Orange: single loading to 60% of maximum stress and relaxation. Blue: sequential loading and relaxation to 80% of maximum strain.

the hoof wall. Following the hydration control process, measurements were taken to quantify how moisture affects the volume of the hoof wall. It was found that as samples were hydrated from 0% to 15% water content, there was an increase in the volume of about 13%. With this increase in volume, the width and thickness experience the most change, 6% and 4%, respectively, whereas little change (just 2%) occurred along the height (longitudinal direction). This could be due to the IF orientation; when

water molecules penetrate materials composed of alpha-helices with crystalline IFs, the nanoscale matrix that the IFs are embedded in absorbs water and expands while the IFs remain largely unchanged.^[32] Thus, the material is expected to expand more perpendicular to the IF orientation.

Figure 12c shows four hoof samples that were all compressed to 60% strain and allowed to relax in four different conditions. For water immersed relaxation, sequentially and monotonically

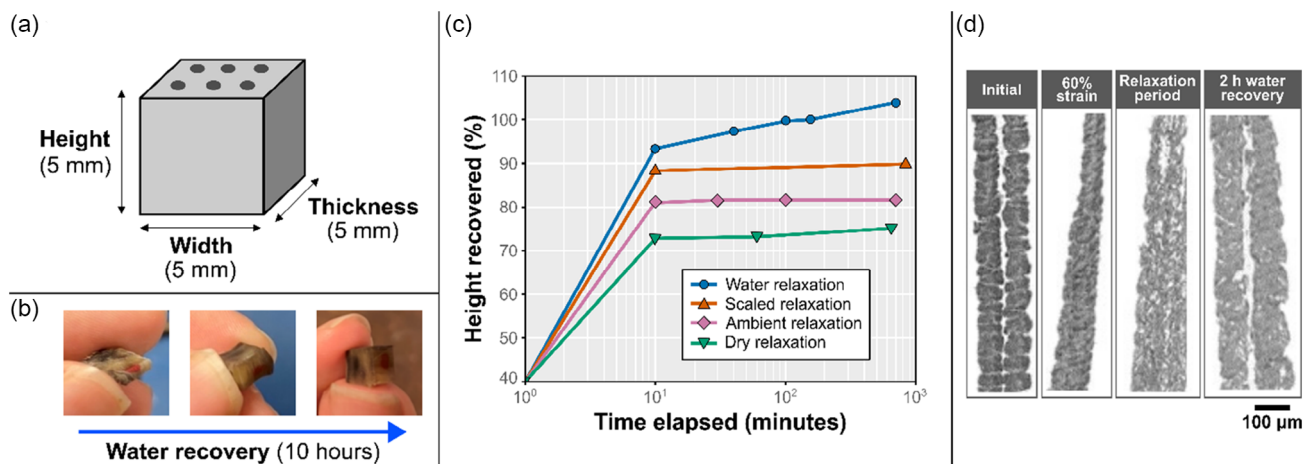


Figure 12. a) Schematic of hoof wall sample dimensions used for 4D microcomputed tomography (microCT) experiments; b) compressed hoof wall sample's macroscopic recovery when submerged in water over a 10 h period; c) plot of % height recovered vs. time elapsed (min) on log scale of relaxation samples; and d) MicroCT scans of the water relaxation sample at its initial state, 60% strain state, after 5 min of relaxation, and after 2 h of water submergence relaxation.

loaded samples were initially hydrated to 15% water content prior to testing. The sequentially loaded sample was compressed in increments of 20% strain with relaxation periods between loadings. After testing, the sequentially and monotonically loaded relaxation samples were left out in ambient conditions, whereas the water relaxation sample was submerged in water. The dry relaxation sample had near 0% water content before testing. After testing, the dry relaxation sample was left out in ambient conditions. Of the four samples, the water relaxation sample appears to have fully recovered, even regaining 103.8% of its original height after 10 h of water recovery. Additionally, a tomograph of the water-relaxed sample cavity is shown in Figure 12. At 60% strain, the two depicted tubules bend significantly as bridges between cavity pockets begin to collapse. After the relaxation period, the tubules restraighten. After recovering in water for 2 h, the tubules regain their original shape and detail. The sequentially loaded relaxation sample performed better than the monotonically loaded relaxation sample recovering 10% more of its height than the monotonically loaded sample by

the end of the experiment. Within the first few minutes of recovery, all samples regained at least 70% of their initial shape.

3.3. Fracture Behavior

One of the most intriguing mechanical aspects of the hoof wall is the ability of its structure to control fracture behavior. Several design strategies are utilized to accomplish this, including varying the intermediate filament orientation and using the weak planes between them in the intertubular region to redirect cracks away from the living tissue inside the hoof wall.^[2] The tubules, however, also play a key role, particularly in the innermost and outermost regions of the hoof, where cracks prefer to propagate along tubule interfaces with the matrix.^[7] This observation was determined from post-fracture imaging on compact tension specimens. Post-impact fractography showed that tubules redirected cracks, causing tortuous crack paths and that the tubules can even act as crack bridges and arresters.^[8] The following section uses compact tension tests to detail fracture behavior in the hoof as cracks propagate.

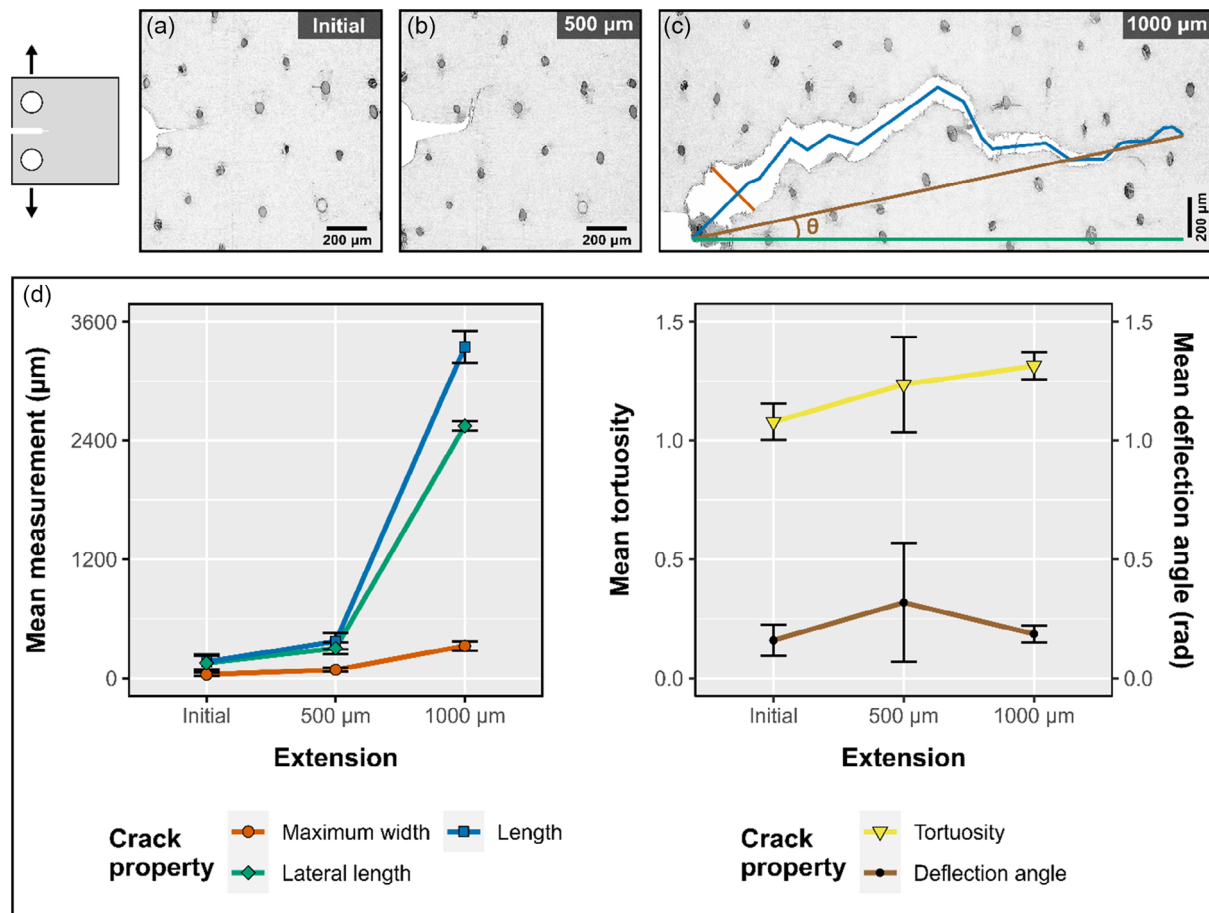


Figure 13. a–c) Images extracted from a series of microcomputed tomography (microCT) scans showing crack propagation within the hoof wall under ambient conditions. The number in the top right indicates the crosshead extension distance for the compact tension samples. (c) Procedure for taking crack measurements; the blue line shows how the crack length was measured, while the green line measures the lateral distance that the crack has traveled through the sample. The ratio of these lines indicates how tortuous the crack path is. The brown line indicates the angle of deflection, θ , from the start of the crack to the end and the orange line measures the maximum crack width; and d) plots of crack measurements at the different extension values (error bars represent standard deviation of the mean; $n = 40$ measurements for each scan).

3.3.1. Effect of Structure

Several toughening mechanisms suggested by previous authors were confirmed with periodic microCT. For example, the tortuous crack paths that arise from the tubule architecture can clearly be seen in **Figure 13**. To capture the tortuosity of the fracture, the centerline of the crack was traced (shown in blue) and measured and compared to the total lateral distance (shown in green) traveled by the crack. The ratio of these two values was calculated from measurements at 35 evenly spaced slices through the thickness of the sample, giving an average value of 1.24 and 1.32 at 500 and 1000 μm extension, respectively. This result suggests that the deflection caused by the tubules increases crack length by approximately 20–30%. This is $\approx 10\%$ higher than that of the hoof-inspired 3D-printed samples tested by Lazarus et al.^[8]

One reason for this increase in tortuosity could be the mechanism by which the tubules cause crack deflections. In the simplified 3D-printed samples, cracks travel through the intertubular material until a tubule is encountered. Then, the crack deflects around the tubule before continuing to travel straight. The hoof tubules, however, appear to capture approaching cracks, even ones that appear to be passing by harmlessly. Here, it seems that the crack is attracted to the tubule and is “pulled” into the plane of weakness between the microscale tubular cortical layers rather than being redirected at the mesoscale interface between the tubules and intertubular material. A prime example of this behavior can be seen in the first two panels of **Figure 14**. The introduced precrack begins just below the tubule. In printed samples, this crack would likely deflect slightly down, away from the stiff tubular material, and then continue traveling to the right

once it had passed the reinforced cortex (**Figure 14**, lower left panel). In the hoof sample, it gets pulled toward the tubule, curling behind it (**Figure 14**, top right panel). This is likely the result of the crack getting trapped in the planes of weakness between the cortical layers that surround the medullary cavity. These layers can be seen forming fiber bridges behind the crack tip, an extrinsic toughening mechanism well known to improve fracture toughness,^[33,34] as the fracture attempts to continue moving laterally through the sample. In the bottom right panel of **Figure 14**, multiscale crack bridging can be observed, with both whole tubules and smaller fibers spanning the crack wake. This crack deflection mechanism in the hoof samples leads to a lower angle of deflection ($\approx 10.5^\circ$ after 1000 μm of extension) relative to bioinspired designs, which saw angles of deflection between 11° and 18° after interacting with a similar number of tubules.^[35]

3.3.2. Effect of Hydration

Moisture has a large effect on the mechanical properties of keratin. When water molecules infiltrate keratinous materials, they disrupt the hydrogen bonds that stabilize the alpha helices and weakly cross-link adjacent polymer chains. The result is a dramatic decrease in stiffness and an increase in ductility. During the fracture events, this ductility causes a significant amount of crack blunting. **Figure 15** shows the crack tip of a hydrated sample during compact tension testing.

Unlike the samples tested in drier conditions, the structure of the hoof plays a much smaller role in the crack progression. The tortuosity remains near 1, and the crack deflection angle drops to

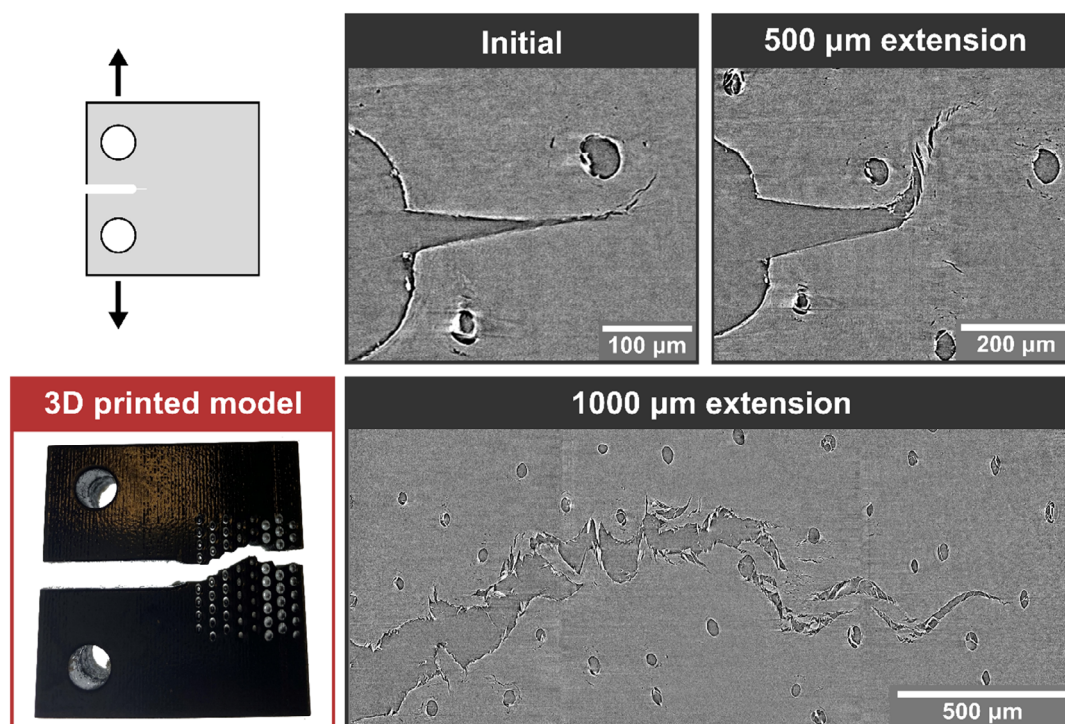


Figure 14. Microcomputed tomography (microCT) scans showing the crack deflection mechanism of the tubule region, which “pulls” cracks in and trap them in the planes of weakness between the helical cortical layers of cells surrounding the medullary cavity.

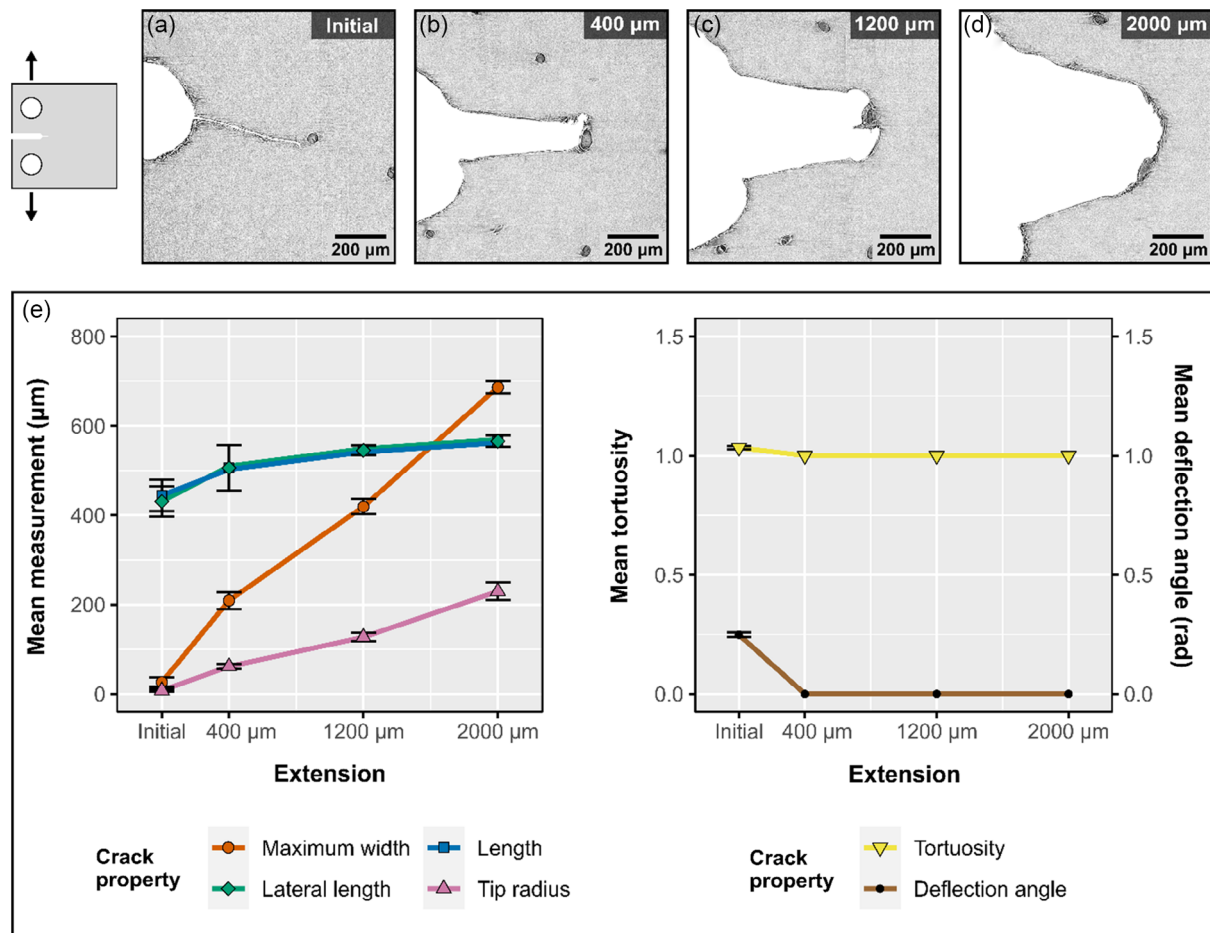


Figure 15. Hydrated hoof samples exhibit significant crack blunting. This can be seen by the increasing radius of curvature of the crack tip, while the crack length stays relatively the same. a–d) Images extracted from a series of microcomputed tomography (microCT) scans of hydrated samples at different extensions during compact tension test; and e) plots of the properties of the crack as it grows during testing (error bars represent standard deviation of the mean; $n = 40$ measurements for each scan).

0° as the crack travels straight through the sample. The crack length changes only marginally as the sample is pulled apart while the crack width and tip radius increase dramatically.

3.4. Study Limitations

While periodic microCT offers powerful insight into the behavior of the hoof wall's microstructure during loading, there are several limitations to this technique. The first limitation is that not all of the features in the hoof can be easily visualized with this approach. The most observable structures are regions with large differences in X-ray absorption, for example, hollow regions vs. nonhollow regions. However, important structures, such as the intertubular lamellae, play an important role in the hoof wall's behavior but were not explored in this study. Another limitation lies in the requirement that specimens are held still during scanning. This limits the mechanical portion of the experiments so that samples cannot be steadily loaded but instead have periods of relaxation during testing. Finally, while periodic scans do provide information on sample behavior, there are inevitably gaps between each snapshot. Future experiments on the *in situ*

behavior of the hoof wall or even other keratinous materials can build off the results in this study to focus on the most interesting strain ranges of deformation.

4. Conclusions

The horse hoof is a remarkable structural biological material with unique failure and hydration-induced shape recovery mechanisms. In this study, periodic microcomputed tomography scans were used to explore the mechanisms, at both the meso and microscale, that are responsible for this outstanding performance. Experiments coupled with mechanical tests and characterization compliment the findings of earlier studies^[4,8,18,19] and provide new insights into the hoof wall's structure.

Several conclusions are drawn regarding the compressive behavior of the hoof wall's structure: 1) a significant fraction of the tubules in the hoof wall tends to have a wavy structure that acts as a guide for how buckling occurs during compression. No kinking/lateral cracking was observed in the tubule walls, likely due to the fibrous and more ductile (relative to engineered

composite materials) nature of the hoof wall. This feature allows the reinforcing elements to continue resisting loading even after significant deformation, improving the material's toughness; 2) the medullary cavities are collapsible features that absorb strain energy and endure plastic damage before the rest of the hoof wall; 3) regions with less tubule bridging were observed to collapse prior to areas with more bridges, supporting the notion that tubule bridges stabilize the medullary cavity; 4) hydrated samples exhibited tubule buckling and collapsed while dry samples cracked, often along an axis diagonal to the tubules. This might be due to the intertubular fiber orientation, as suggested by Kasapi and Gosline.^[2] Dry samples also showed very little tubule or bridge distortion, while both were significantly deformed in the hydrated samples; and 5) interior tubules collapse sooner than tubules from the exterior while tubules prefer to collapse along the radial axis and densify easier when compressed in this direction. This along with differences in bridge support leads to a cascading failure mechanism where tubules collapse at different strain levels.

Relaxation tests elucidated several key findings regarding the role of the hoof wall's microstructure on its viscoelastic behavior: 1) samples loaded sequentially reached a maximum stress 46% lower than that of samples loaded monotonically and exhibited more tubule bending and less cavity collapse. This highlights the dissipative viscoelastic response of the hoof wall, which can be beneficial in preventing the build-up of stress in the hoof during locomotion; 2) after relaxation, compressed samples displayed noticeable shape recovery, including collapsed cavities reopening and tubule restraightening; and 3) hydration significantly enhanced shape recovery. Full submersion in water provided maximum recovery. This self-healing capability is an important attribute of hooves.

Finally, compact tension tests were used (extending previous studies^[2,4,5,7,8]) to probe the fracture behavior of the hoof wall. Previous findings were verified, and new observations regarding how cracks propagate through the hoof were identified: 1) the previously proposed mechanisms of crack deflection^[2,4,5,7,8] were experimentally verified during propagation. Cracks traveling near tubules are pulled inward, becoming trapped within the helical, cortical planes that compose the tubular regions. To continue traveling laterally through the hoof wall, cracks need to propagate through these fibrous lamellae. Thus, bridging cracks are formed. Similarly, intertubular fibers and even entire tubules were seen bridging crack wakes, introducing an extrinsic toughening mechanism on multiple hierarchical levels that resists further crack extension and enhances the toughness; 2) measurements of the crack length showed that this tubular deflection mechanism causes significantly longer and more tortuous fracture paths; and 3) hydration has an important effect on crack propagation, causing significant crack tip blunting. When very hydrated, the structure of the hoof wall shows no discernable effect on crack propagation.

Acknowledgements

B.S.L. and R.K.L. contributed equally to this work. The authors acknowledge funding from the National Science Foundation Mechanics of Materials and Structures program (Grant Nos. 1926353 and 1926361).

The late Professor Joanna McKittrick was an inspiring influence on this project, and her contributions were vital to this publication. The authors would like to thank D.P., H.B., and D.P. at the Advanced Light Source beamline 8.3.2 at Lawrence Berkeley National Laboratory for their help performing and reconstructing the microcomputed tomography scans. The authors would also like to thank BNM for his help with transmission electron microscopy imaging of the hoof wall.

Conflict of Interest

The authors declare no conflict of interest.

Data Availability Statement

The data that support the findings of this study are available from the corresponding author upon reasonable request.

Keywords

equine hooves, keratin, periodic microcomputed tomography, stress relaxation, tubular structures

Received: December 22, 2022

Revised: April 11, 2023

Published online:

- [1] B. S. Lazarus, A. Velasco-Hogan, T. Gómez-del Río, M. A. Meyers, I. Jasiuk, *J. Mater. Res. Technol.* **2020**, *9*, 15705.
- [2] M. A. Kasapi, J. M. Gosline, *J. Exp. Biol.* **1997**, *200*, 1639.
- [3] W. Huang, *PhD Thesis*, University of California San Diego **2018**.
- [4] W. Huang, N. A. Yaraghi, W. Yang, A. Velazquez-Olivera, Z. Li, R. O. Ritchie, D. Kisailus, S. M. Stover, J. McKittrick, *Acta Biomater.* **2019**, *90*, 267.
- [5] M. A. Kasapi, J. M. Gosline, *J. Exp. Biol.* **1999**, *202*, 337.
- [6] J. E. Bertram, J. M. Gosline, *J. Exp. Biol.* **1986**, *125*, 29.
- [7] M. A. Kasapi, J. M. Gosline, *J. Exp. Biol.* **1996**, *199*, 1133.
- [8] B. S. Lazarus, R. K. Luu, S. Ruiz-Pérez, W. B. A. Bezerra, K. Becerra-Santamaria, V. Leung, V. H. L. Durazo, I. Jasiuk, J. D. V. Barbosa, M. A. Meyers, *Acta Biomater.* **2022**, *151*, 8205.
- [9] J. D. Reilly, D. F. Cottrell, R. J. Martin, D. Cuddeford, *Biomimetics* **1996**, *4*, 23.
- [10] C. C. Pollitt, *Equine Vet. Educ.* **1998**, *10*, 318.
- [11] M. A. Kasapi, J. M. Gosline, *Equine Vet. J.* **1998**, *30*, 10.
- [12] M. K. Habibi, A. T. Samaei, B. Gheshlaghi, J. Lu, Y. Lu, *Acta Biomater.* **2015**, *16*, 178.
- [13] G. Chen, H. Luo, *Compos. Commun.* **2021**, *24*, 100647.
- [14] S. Amada, Y. Ichikawa, T. Munekata, Y. Nagase, H. Shimizu, *Composites, Part B* **1997**, *28*, 13.
- [15] F. Nogata, H. Takahashi, *Compos. Eng.* **1995**, *5*, 743.
- [16] F. L. Palombini, W. Kindlein, B. F. de Oliveira, J. E. de Araujo Mariath, *Mater. Charact.* **2016**, *120*, 357.
- [17] J. Thomason, A. Biewener, J. Bertram, *J. Exp. Biol.* **1992**, *166*, 145.
- [18] J. E. Douglas, C. Mittal, J. J. Thomason, J. C. Jofriet, *J. Exp. Biol.* **1996**, *199*, 1829.
- [19] D. H. Leach, *PhD Thesis*, University of Saskatchewan **1980**.
- [20] N. Akbari Shakhosravi, S. Gohari, A. Komeili, C. Burvill, H. Davies, *J. Mech. Behav. Biomed. Mater.* **2021**, *121*, 104622.
- [21] C.-S. A. Shiang, C. Bonney, B. Lazarus, M. Meyers, I. Jasiuk, *J. Mech. Behav. Biomed. Mater.* **2022**, *136*, 105529.

- [22] T. N. Sullivan, Y. Zhang, P. D. Zavattieri, M. A. Meyers, *Adv. Funct. Mater.* **2018**, 28, 1801250.
- [23] W. Huang, A. Zaheri, W. Yang, D. Kisailus, R. O. Ritchie, H. Espinosa, J. McKittrick, *Adv. Funct. Mater.* **2019**, 29, 1901077.
- [24] J. E. Bertram, J. M. Gosline, *J. Exp. Biol.* **1987**, 130, 121.
- [25] J. Schindelin, I. Arganda-Carreras, E. Frise, V. Kaynig, M. Longair, T. Pietzsch, S. Preibisch, C. Rueden, S. Saalfeld, B. Schmid, J.-Y. Tinevez, D. J. White, V. Hartenstein, K. Eliceiri, P. Tomancak, A. Cardona, *Nat. Methods* **2012**, 9, 676.
- [26] J. Ollion, J. Cochenec, F. Loll, C. Escudé, T. Boudier, *Bioinformatics* **2013**, 29, 1840.
- [27] H. Wickham, *Ggplot2: Elegant Graphics for Data Analysis*, Springer-Verlag, New York **2016**.
- [28] R Core Team, *R: A Language and Environment for Statistical Computing*, R Foundation for Statistical Computing, Vienna, Austria **2022**, <https://www.r-project.org/>.
- [29] B. Budiansky, N. A. Fleck, *J. Mech. Phys. Solids* **1993**, 41, 183.
- [30] J. Lankford, *J. Mater. Sci.* **1995**, 30, 4343.
- [31] I. Chung, Y. Weitsman, *Int. J. Solids Struct.* **1995**, 32, 2329.
- [32] D. S. Fudge, J. M. Gosline, *Proc. R. Soc. London, Ser. B* **2003**, 271, 291.
- [33] U. G. K. Wegst, H. Bai, E. Saiz, A. P. Tomsia, R. O. Ritchie, *Nat. Mater.* **2015**, 14, 23.
- [34] R. Khan, *Compos. Struct.* **2019**, 229, 111418.
- [35] B. S. Lazarus, R. K. Luu, S. Ruiz-Pérez, W. B. A. Bezerra, K. Becerra-Santamaria, V. Leung, V. H. L. Durazo, I. Jasiuk, J. D. V. Barbosa, M. A. Meyers, unpublished results **2022**.